ELSEVIER

Surface Science 480 (2001) 153–162

SURFACE SCIENCE

www.elsevier.nl/locate/susc

Element-selective mapping of magnetic moments in ultrathin magnetic films using a photoemission microscope

W. Kuch [a,*], J. Gilles [a], F. Offi [a], S.S. Kang [a], S. Imada [b], S. Suga [b], J. Kirschner [a]

[a] *Max-Planck-Institut für Mikrostrukturphysik, Weinberg 2, D-06120 Halle, Germany*
[b] *Graduate School of Engineering Science, Osaka University, 1–3 Machikaneyama, Toyonaka 560-8531, Japan*

Abstract

We combine X-ray magnetic circular dichroism (XMCD) and photoelectron emission microscopy to obtain locally resolved magnetic information on a microscopic scale. Scanning the photon energy across elemental absorption edges and recording microscopic images of the local secondary electron intensity for both photon helicities at each photon energy step allows to analyze local XMCD spectra at any position of the imaged area of the sample. With the help of magnetic sum-rules local quantitative information about magnetic moments can be extracted from such microspectroscopic measurements. The full power of XMCD as a spectroscopic tool is so maintained, while microscopic spatial resolution is added. © 2001 Elsevier Science B.V. All rights reserved.

Keywords: Photoemission (total yield); Photoelectron emission; X-ray absorption spectroscopy; Iron; Nickel; Magnetic films

1. Introduction

The study of ultrathin magnetic structures and multilayers has recently attracted considerable interest, fueled by the prospect of technological applications in the fields of high density magnetic data recording, magnetic sensors, non-volatile magnetic random access memory, and spin electronics in general. The rapidly decreasing size of such magnetic structures calls for experimental techniques that allow the study of magnetic properties on a microscopic scale. Photoelectron emission microscopy (PEEM) is one such technique that has already proven its versatility for the imaging of magnetic domains in ultrathin films [1–3]. Magnetic circular dichroism in soft X-ray absorption (XMCD) serves as mechanism for magnetic contrast. The absorption of circularly polarized X-rays at elemental absorption edges depends on the relative orientation of sample magnetization and light helicity [4,5]. In PEEM a magnified image of the secondary electron intensity distribution at the sample surface is generated in a parallel way. The secondary electron intensity distribution under exposure to X-rays is a measure of the local X-ray absorption. In practice two images for opposite light helicity of the circularly polarized light at the maximum of the absorption edge are acquired and subtracted in order to separate magnetic from topographical contrast. This method has been successfully employed for the study of magnetic thin films, microstructures, and exchange coupled systems [2,3].

* Corresponding author. Tel.: +49-30-6392-4927; fax: +49-30-6392-4984.
E-mail address: kuch@bessy.de (W. Kuch).

0039-6028/01/$ - see front matter
PII: S0039-6028(01)00830-5

The full power of XMCD lies in its spectroscopic information. Sum-rules [6,7] have been proposed to deduce quantitative magnetic information from the difference curve between photon energy scans for opposite light helicity. XMCD has since then developed into a widely used technique for the element-specific characterization of magnetic thin films and multilayers [8,9]. Although there has been some dispute about the applicability of these sum-rules [10,11], they seem to yield reasonable results for the 3d transition metals [8,9,12]. These sum-rules allow one to extract the spin and orbital magnetic moments from the evaluation of the integrated cross section at the L_3 and L_2 edges of transition metals for opposite light helicity, thereby enabling the separate determination of magnetic moments of different elements in the same sample.

A rather important point is the element-specificity of XMCD–PEEM, since in many materials for technological application the effects of magnetic coupling and/or electric transport between different magnetic layers are employed. By tuning the exciting X-ray radiation to the different absorption edges, a separate determination of the magnetically active layers is possible, if different elements are contained.

With the improved brilliance of radiation from third generation synchrotron light sources the acquisition times for PEEM images have become short enough to combine the microscopic information of PEEM and the spectroscopic information of XMCD in the most consequent way. This implies to scan the photon energy in small steps and record complete microscopic images of the secondary photoelectron intensity for both photon helicities at each step (full-image microspectroscopy), not only at the absorption maximum. From such a data set the analysis of local XMCD spectra at any position of the image is possible. The full quantitative information inherent to XMCD can thus be extracted with the spatial resolution given by the imaging process. Sum-rule analysis for every single pixel in the image does then result in microscopic maps of orbital and spin moments. This can be of the highest importance for the study and the understanding of micromagnetic aspects of magnetic anisotropy or magnetic interlayer coupling. Since the magnetocrystalline anisotropy manifests itself in an anisotropy of the orbital moment [13,14], even microscopic measurements of the angular dependence of magnetic anisotropies in an element-selective way may become possible.

In this contribution we demonstrate the practicability of this kind of microspectroscopy, and present examples of full-image XMCD–PEEM microspectroscopy. The setup and the carrying out of the experiments is described for the microscopic mapping of magnetic moments in microwedges of epitaxial magnetic films on a single crystal Cu(0 0 1) sample. Special emphasis is put on corrections to the data that are specific to imaging spectroscopy. A procedure for a simplified sum-rule analysis is presented that allows the automatic analysis of a large amount of XMCD data. Results for images of orbital and spin moments are shown for Fe in Ni/Fe/Co/Cu(0 0 1) and Ni in Co/Ni/Cu(0 0 1).

2. Experiment

The experiments were performed using circularly polarized synchrotron radiation emitted in the first harmonic from the twin-helical undulator beamline for soft X-ray spectroscopy BL25SU [15,16] of SPring-8 in Japan. After having set the two undulators to opposite helicity, helicity reversal was realized by closing one undulator and fully opening the other. The degree of circular polarization is $>98\%$. The light was incident to the sample under a grazing angle of 30° from the sample surface.

The setup of the photoemission microscope (Focus IS-PEEM [17]) is identical to that described in previous publications [3]. In short, it consists of a three-lens electrostatic straight optical axis microscope with an integral sample stage and a variable contrast aperture. The magnified image is intensified by a two-stage microchannel plate, and converted into visible light by means of a scintillator crystal. The image is then computer-recorded with 12-bit resolution by a Peltier-cooled camera (PCO SensiCam [18]). The binning of camera pixels was adjusted to have exposure times of

single images of not more than 30 s, in order to achieve reasonable acquisition times for the complete spectral series of images. For the data presented here 4×4 and 8×8 binning was used. The width of the energy steps in the scans at the Ni $L_{2,3}$ edges was set to 0.65 eV before the L_3-edge and in between the L_3 and L_2 peaks, 0.26 eV near the L_3 peak, 0.34 eV near the L_2 peak, and 1.4 eV in the post-L_2 region. For the scans at the Fe $L_{2,3}$ edges a constant stepwidth of 0.22 eV was used.

Special attention has to be paid in microspectroscopy to the normalization of the local spectra to the incoming photon flux. In integral absorption spectroscopy this is usually easily achieved when simultaneously the absorption signal from the sample and the photoyield of a monitor is recorded. This can be a grid in the incoming photon beam, or an optical element such as a mirror. Since the entire photon beam is contributing to both the monitor signal and the signal from the sample, normalization is straightforward. In imaging microspectroscopy, however, the local, pixel-resolved, photon flux density cannot be measured, and may deviate significantly from the integral photon flux signal of such a monitor. An inhomogeneous distribution of the photon intensity within the imaged area on the sample invalidates the normalization to a conventional beam monitor. A further complication arises from the fact that the intensity distribution within the light beam from an undulator is also photon energy dependent.

In order to reduce the influence of these inhomogeneities, it is necessary to reduce the lateral extension of the light spot to not much more than the area imaged in the microspectroscopic measurement. This excludes portions of the X-ray beam that are irrelevant for the measurement from contributing to the monitor signal. It can be achieved by using appropriate apertures in the beamline. In beamline optics where the light spot is an image of the exit slit, reducing the exit slit width also reduces the illuminated area. Attention should also be paid to the adjustment of the imaged area to the center of the undulator radiation. After careful adjustment on BL25SU, the remaining deviation between the integral photon flux measured at the last optical element, a gold-coated refocusing mirror, and the local photon flux could be reduced to less than 5–7%. It was determined from the correction procedure described in the next section.

Co, Ni, and Fe films were evaporated at room temperature by electron bombardment of high purity rods. Deposition rates were calibrated from the oscillations in specular medium energy electron scattering intensity during deposition. Typical deposition rates were between 0.3 and 0.7 ML/min. Wedge-shaped films were prepared by placing an aperture of 2×0.5 mm^2 in front of the sample. The distance to the sample surface could be varied between 1 and 1.5 mm. During deposition the sample-mask assembly was rocked by up to $\pm 7.5^\circ$ about the long axis of the aperture. This results in stripes with a thickness plateau in the middle and wedges with a width in the range of 200–300 μm on both sides. After changing the sample azimuth by 90°, a second stripe could be prepared perpendicular to the first one, resulting in four regions of perpendicularly crossed wedges.

3. Data analysis

Fig. 1(a) shows raw Fe $L_{2,3}$ XMCD data of a single camera pixel in 8×8 binning mode, displaying the averaged information from a 3×3 μm^2 area of a bilayer of 10 atomic monolayers (ML) Fe and 6 ML Co on Cu(0 0 1). Spectra for positive and negative helicity are depicted by solid and dotted lines, respectively. The two peaks correspond to the Fe L_3 and L_2 absorption maxima. The acquisition time per image, i.e., per data point, was 10 s. The sample had been magnetized previously in the light incidence azimuth, which coincided with the substrate [1 1 0] crystallographic direction.

The corresponding monitor signal, representing the integral photon flux, is displayed in Fig. 1(b). The intensity for light of negative helicity, which was provided by the downstream undulator, is about 20–25% higher than that of the upstream undulator because of the shorter distance between source and pinhole aperture. It is also seen that the energetic position of the maxima of the harmonics are slightly different, with the maximum for negative helicity being about 4 eV higher in energy.

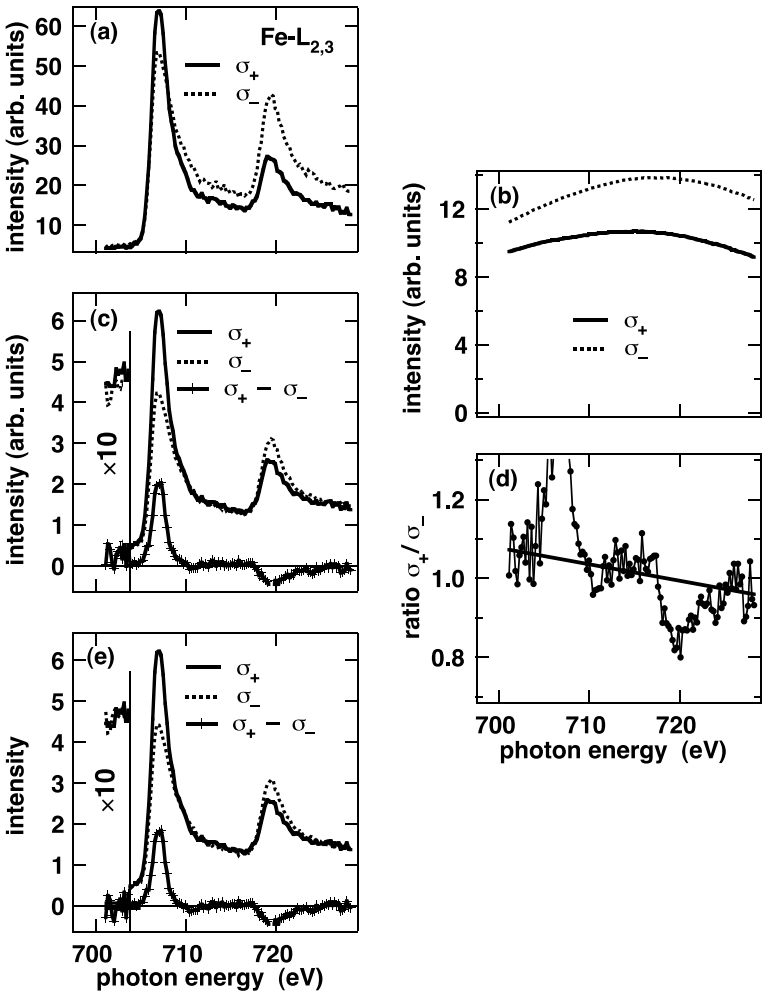

Fig. 1. Example for the correction of single pixel XMCD data of 10 ML Fe/6 ML Co/Cu(0 0 1). Curves for positive (negative) helicity are shown as solid (dotted) lines. (a) Raw data from a 3×3 μm^2 area of the sample. (b) Integral photon flux as measured from the photoyield of the last mirror. (c) Data of (a) corrected by the curves of (b). The difference between the two curves is also shown in the bottom. (d) Ratio of the two spectra of (c). The straight line is a linear fit to the data disregarding the peak regions. (e) Spectra from (c) after multiplying the curve for negative helicity by the straight line of (d). Also shown is the difference curve. The pre-edge region for photon energies below 704 eV is shown scaled by a factor of 10 in intensity in panels (c) and (e) for a better visualization of the alignment of the spectra.

Fig. 1(c) shows the spectra of panel (a) after normalization to the integral photon flux of panel (b). At the bottom of Fig. 1(c) the difference between the two spectra is presented. It shows the well-known magnetic circular dichroism with a positive difference at the L_3 edge, and a negative signal at the L_2 edge. The leftmost part of the figure ($<$704 eV) is magnified by a factor of 10 in intensity. Note that here the solid and dotted lines at $\approx$4.5 intensity units belong to the absorption curves, which display a pre-edge intensity of $\approx$0.45 intensity units, whereas the data points slightly above the zero line belong to the difference curve. The small residual differences between the two spectra in the pre-edge region seen in the magnified part of Fig. 1(c) are caused by differences between

the integral photon flux of panel (b) and the unknown local photon flux at the position in the image from where the spectra were taken. To correct these differences, the following procedure was adopted: First the ratio (intensity for positive helicity divided by intensity for negative helicity) of the normalized spectra of Fig. 1(c) was calculated. It is displayed in Fig. 1(d). Here it is seen that outside the absorption peaks the ratio between absorption of X-rays with positive and negative helicity is not exactly one, as it should be. The reason are inhomogeneities in local photon flux density, as described in the previous section. Because the energy relative to the respective maximum of the undulator harmonics is different in the two scans for opposite helicity, also the deviation from a ratio of one is energy-dependent. For the correction a linear energy dependence is assumed. It is obtained from a fit of a straight line to the ratio of Fig. 1(d). The peak regions exhibiting the magnetic dichroism are excluded before fitting. The result of the linear fit is then used to correct the single pixel spectra. In Fig. 1(d) this correction varies between $+7.0\%$ at the left-hand side, and -3.8% at the right-hand side. This energetic variation is caused by the energy dependence of the intensity distribution within the light spot of the undulator harmonics. It is narrower for higher energies relative to the peak maximum of the harmonics. In that case the photon flux density in the center of the light spot is higher. From Fig. 1(b) it is seen that the maximum of the undulator harmonics for positive helicity was at slightly lower energies than for negative helicities. The local intensity for positive helicity is consequently higher at the low energy side of the spectra of Fig. 1, since here the energy relative to the maximum is higher than for negative helicity.

The corrected spectra and corresponding difference curve are finally shown in Fig. 1(e). Again the region below 704 eV photon energy is shown magnified by a factor of 10 in intensity. Compared to the magnified part of Fig. 1(c), it is seen that now also in the pre-edge region the spectra overlap perfectly. The correction procedure as described above has been performed for all pixels in an image. Only a smooth variation of the fit parameters for the linear fits was observed within the imaged area. The maximum correction did not exceed 5–7% if care was taken for limiting the excess radiation outside the imaged area to a minimum. The small local variation of the correction can be due to slight deviations in the positions of the central undulator beam on the sample for the two helicities.

Sum-rule analysis can now be performed on the corrected single pixel data. Because of the high number of spectra that have to be analyzed in full-image microspectroscopy this has to be done automatically. A problem is that the data can sometimes be rather noisy, especially at positions where the dichroism is small. In most cases the result of interest in sum-rule analysis is two numbers, namely the spin and orbital moments. They are obtained from summing and subtracting the areas of the difference curve at the L_3 and the L_2 edges, respectively [6,7]. If the line shape of the helicity averaged absorption spectra is assumed to be constant over an image, then an analysis procedure that reduces the spectral information on two independent numbers is sufficient. The following fit procedure was therefore used: First a template XMCD spectrum with a sufficiently good statistics is generated by summing over a large area. This spectrum was then analyzed as described in more detail in Refs. [8,9,19]. All the corrected single pixel spectra are normalized on a per-atom basis by setting the intensity axis to zero before the $L_{2,3}$ edge, and to one above the edge. The template difference curve was then fitted to the single pixel difference curves. For this it was separated into two parts representing the dichroism at the L_3 and the L_2 edge. If the dichroism spectra at the L_3 and the L_2 edges individually keep their shape and only vary in size, a perfect fit is obtained by just independently scaling the two parts of the template difference curve. This was checked to be the case for the spectra presented here. The result of the fit are the two scaling factors that are needed to fit these two parts of the template difference curve to the single pixel difference curve. These two numbers can be directly converted into numbers for the spin and orbital moments of the single pixel XMCD spectrum, using the information from the analysis of the template spectrum. By

using only two fit parameters connected to the dichroism intensity at the L_3 and L_2 edge, the fit procedure is very stable, which is a prerequisite for obtaining meaningful information from noisy or scattered single pixel data. In addition, it is also easily programmed to run automatically over a large number of spectra.

Fig. 2(a)–(f) show examples of such a template fit procedure for three single pixel spectra of the Fe $L_{2,3}$ edges in Ni/Fe/Co/Cu(0 0 1). The Co thickness

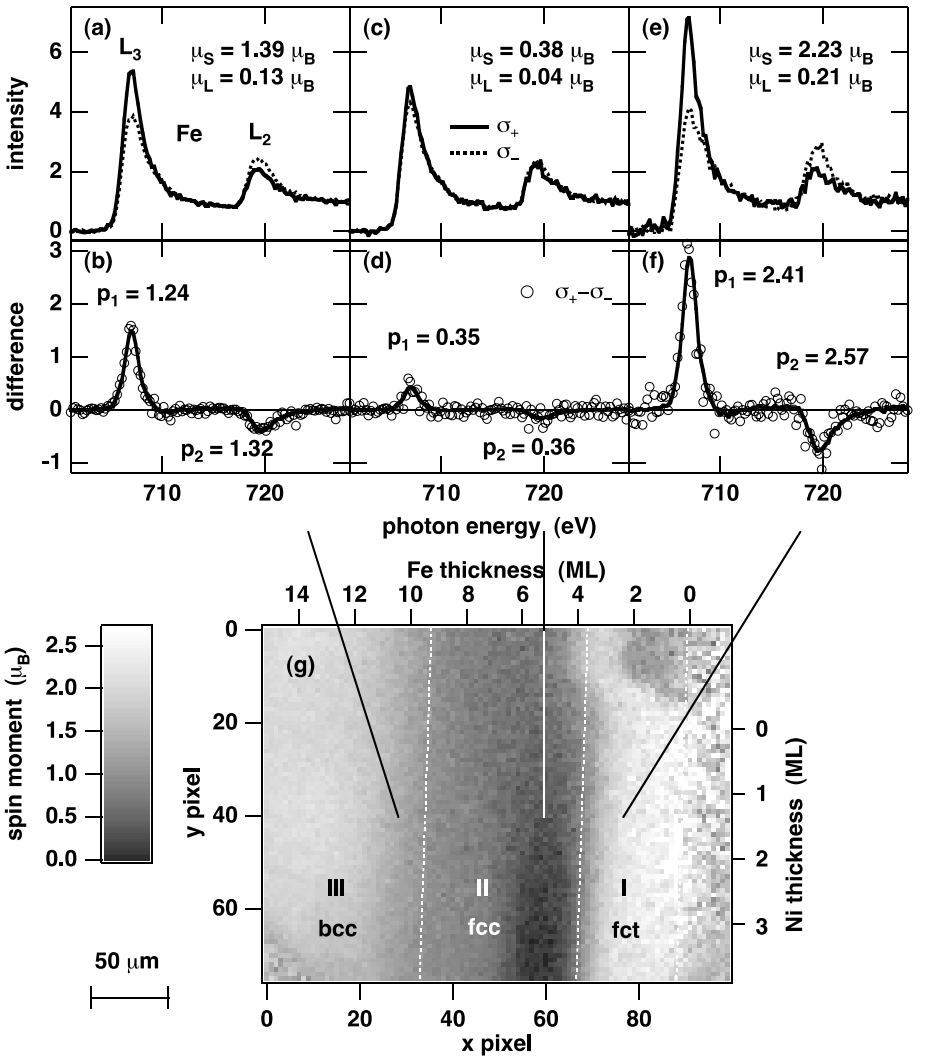

Fig. 2. Example for the sum rule analysis of single pixel XMCD spectra. (a), (c), (e): Corrected single pixel absorption spectra at the Fe $L_{2,3}$ edges in 1.2 ML Ni/x ML Fe/6 ML Co/Cu(0 0 1) for positive (solid lines) and negative helicity (dotted lines). (b), (d), (f): Difference between spectra for opposite helicity of panels (a), (c), and (e) (open symbols). The Fe thickness x is ≈10 ML for (a) and (b), ≈5 ML for (c) and (d), and ≈2 ML for (e) and (f). The solid lines in panels (b), (d), and (f) are portions of a template difference curve, obtained from averaging over a larger area, scaled by the fit parameters p_1 and p_2 at the L_3 and L_2 edges, respectively, to match the single pixel difference data. The spin and orbital moments, calculated from p_1, p_2, and the spin and orbital moments of the template spectrum, are listed in panels (a), (c), and (e). (g): Grayscale map of Fe spin moments as explained on the left hand side of a 0–3.9 ML Ni/0–14 ML Fe crossed double-wedge on 6 ML Co/Cu(0 0 1), composed of pixels of 3×3 μm^2 size. The Fe thickness is given at the top axis, the Ni thickness at the right axis. Three regions with different structural and magnetic properties of Fe are labeled I, II, and III.

was 6 ML, the Ni thickness for the selected pixels ≈1.2 ML, and the Fe thickness ≈10 ML ((a), (b)), ≈5 ML ((c), (d)), and ≈2 ML ((e), (f)). The top panels show the corrected and scaled single pixel absorption spectra for positive helicity (solid lines) and negative helicity (dotted lines). In the lower panels the corresponding difference curves are depicted (open symbols). The solid lines in panels (b), (d), and (f) are the result of fits of the template difference curve to the single pixel difference curves. The scaling factors p_1 for scaling the L_3 dichroism and p_2 for scaling the L_2 dichroism of the template difference curve to the single pixel data are also given. The spin and orbital moments of the image pixels are calculated from p_1, p_2, and the sum-rule analysis of the template spectrum (spin moment 1.1 μ_B, orbital moment 0.1 μ_B). The moments found at the three pixels of Fig. 2 are listed in panels (a), (c), and (e).

4. Results and discussion

The strong variation of the resulting magnetic moments in Fig. 2 can be attributed to different magnetic and structural phases of iron in the Ni/Fe/Co trilayer. Fig. 2(g) shows a complete grayscale map of the Fe spin moments of a Ni (0–3.9 ML)/Fe (0–14 ML)/Co (6 ML)/Cu(0 0 1) crossed double-wedge sample. It is composed of 7600 pixels of 3×3 μm^2 size. The positions where the three example single pixel spectra of panels (a)–(f) have been taken are marked by the ends of the three straight lines. The legend for the conversion of the grayscale to magnetic moments is given on the left-hand side. The image shows a section of the double-wedge of Ni and Fe that includes the onset of both wedges. The Fe thickness increases from right to left as indicated at the top axis, the Ni thickness increases from top to bottom as indicated at the right-hand axis. It is seen that the three example single pixel spectra of the top panels have been chosen to represent three regions with rather different Fe spin moments. These regions are separated by white dotted lines, and labeled I, II, and III. Whereas region I exhibits Fe spin moments of $\approx 2.5\mu_B$, the moments in region II are significantly lower. In region III the spin moment increases again from right to left to $\approx 2\mu_B$. In accordance with previous studies of Fe/Co/Cu(0 0 1) [20–22] and Fe/Cu(0 0 1) [23–25], the lower moments in region II are interpreted with a relaxed fcc phase of Fe containing non-ferromagnetic layers [26]. In region I tetragonally expanded fcc-like Fe (fct) with spin moments of about $2.5\mu_B$ is present, whereas at Fe thicknesses between 9 and 12 ML the Fe is converted into the bcc phase, showing spin moments of $\approx 2\mu_B$.

The two-dimensional mapping of magnetic moments in this Ni/Fe double-wedge on Co/Cu(0 0 1) also allows to observe changes in the Fe spin moment as a function of the Ni overlayer thickness. Such a change is recognized at Fe thicknesses between 4 and 6 ML. Here, the Fe spin moment is dropping to values of nearly zero for Ni thicknesses above ≈1.5 ML. This could be caused by an opposite magnetic orientation of the Fe top and bottom interface layers with non-ferromagnetic layers in between. An antiferromagnetic orientation of the Co and Ni layers in Ni/Fe/Co around 5.5 ML Fe thickness has been observed indeed [26]. The observed spin moments have to be interpreted as the depth-weighted average of all Fe layers, where the probing depth over which the secondary electron signal is reduced by a factor of $1/e$ is ≈17 Å [27]. Therefore a non-uniform depth distribution of magnetic moments, which most likely is present in region II, cannot be unambiguously determined from the present data. A simple model assuming a constant amount of ferromagnetic Fe at both interfaces plus non-ferromagnetic Fe in between would lead to a decreasing apparent magnetic moment with increasing Fe film thickness, which is not observed here. The situation is therefore probably more complicated, and the influence of surface and interface roughnesses as well as non-collinear moments may have to be considered.

In the previous example a high spatial resolution was not required, since only the distribution of magnetic properties along the wedges was measured. The PEEM was therefore operated at a low extractor voltage (about 200 V) to yield a large field of view. Fig. 3 shows an example of microspectroscopy with a higher resolution. Here the extractor voltage was 10 kV; together with a

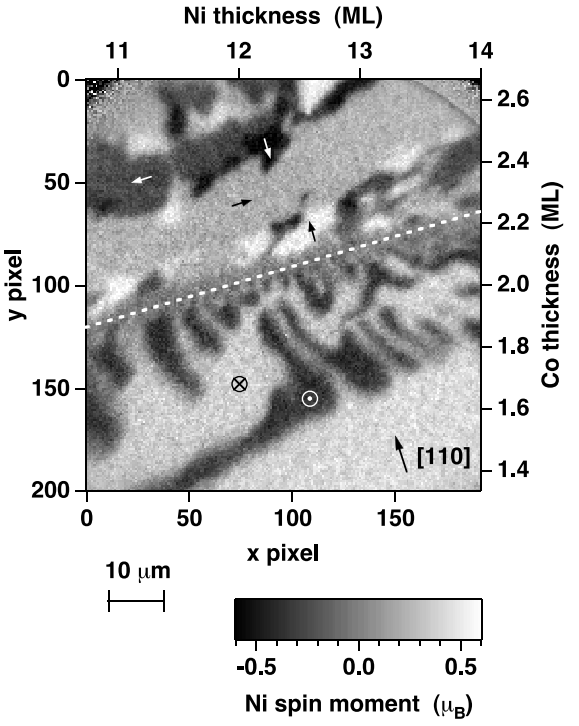

Fig. 3. Map of Ni spin moment projections onto the light incidence direction (from bottom to top, with an angle of 30° to the sample surface) as example for high resolution microspectroscopy. The image is the result of 76 800 single pixel XMCD spectra of 370×370 nm^2, the total data acquisition time of which was about 2 h 20 min. The sample is a Co/Ni/Cu(0 0 1) crossed double wedge. The Ni thickness is indicated at the top axis, the Co thickness at the right axis. The grayscale to magnetic moment conversion is given in the legend at the bottom. The white dotted line separates regions with in-plane magnetization (top) from regions with out-of-plane magnetization (bottom). The magnetization directions are indicated by arrows in some domains.

70 μm contrast aperture this resulted in a resolution of about 500 nm, as determined from linescans across domain boundaries. The pixel size was adjusted to 370×370 nm^2 by using a 4×4 binning of camera pixels. The exposure time per image was 30 s. Fig. 3 displays a section of a Co/Ni crossed double wedge on Cu(0 0 1). In the displayed area the Ni thickness increases from 10.7 to 14 ML from left to right, as indicated at the top axis, and the Co thickness increases from 1.35 to 2.65 ML from bottom to top, as indicated at the right-hand axis. The Ni spin moment as the result of 76800 single pixel XMCD spectra is presented in a grayscale plot. The grayscale to magnetic moment conversion can be seen from the legend at the bottom. Note that here the grayscale is symmetric around zero. Unlike the previous example this sample was not magnetized by an external magnetic field before imaging. The resulting moments from the sum-rule analysis include therefore the cosine of the angle between local magnetization and the helicity of the incident X-rays, which is different for domains of different magnetization direction. It is thus not the absolute value of the spin moment that is obtained from the microspectroscopic analysis, but the projection onto the direction of the incoming light. The light incidence was from bottom to top of Fig. 3, with an angle of 30° to the sample surface.

Two regions with qualitatively different domain structure can be recognized. They are separated in Fig. 3 by the white dotted line. In the upper part of the image four different shades of gray are recognized, namely black, dark gray, light gray, and white. In the lower part only two different shades of gray are found, and the domain boundaries are more rounded. Quantitative analysis of the values of the Ni spin moment projection in the single domains leads to the interpretation that in the upper part of the image the magnetization direction is along the four $\langle 1\,1\,0 \rangle$ in-plane crystallographic directions, as indicated by arrows. The Cu(0 0 1) single crystal substrate was deliberately mounted under an azimuthal angle of 18° between light incidence and the [1 1 0] axis, so that the four $\langle 1\,1\,0 \rangle$ directions all have different projections onto the light incidence direction. In the lower part of the image the values of the spin moment projection and the shape of the domains are consistent with an out-of-plane magnetization. Here the angle between the magnetization axis and the light helicity is 60°. The absolute value of the Ni spin moment is $0.65\mu_B$ over the entire image.

The dotted line in Fig. 3 represents a spin reorientation transition between in-plane and out-of-plane easy axes of magnetization. The spin reorientation transition occurs both as a function of Ni and Co layer thickness. Single films of Ni on Cu(0 0 1) exhibit an out-of-plane anisotropy over an extended thickness range [28–30], whereas Co/Cu(0 0 1) is always in-plane [31,32]. The observed

spin reorientation transition in Co/Ni/Cu(0 0 1) is thus the result of the interplay of Co and Ni anisotropies [33]: for high Ni thickness and low Co thickness the out-of-plane Ni anisotropy dominates, increasing the Co thickness and lowering the Ni thickness the in-plane contribution of the Co film wins.

Interesting is the domain shape in the out-of-plane region close to the spin reorientation transition: As the spin reorientation transition is approached, more and more oppositely magnetized domains are formed. This can be explained by the competition between the magnetostatic energy on the one hand, and the energy cost for creating domain walls on the other hand. Closely spaced alternatingly up and down magnetized perpendicular domains have a lower magnetostatic energy than a single out-of-plane domain due to partial flux closure [34]. The formation of such domains can be energetically favorable close to the spin reorientation transition [35] because at that point the anisotropy energy and hence the energy for the formation of domain walls (in which an in-plane component of the magnetization is present) is low.

5. Summary and conclusion

A practical method for element-selective microscopic mapping of magnetic moments by full-image XMCD microspectroscopy using a PEEM has been described. Spin and orbital moments are obtained from sum-rule analysis of single pixel XMCD spectra of a photon energy series of microscopic PEEM images. This has been applied to Ni/Fe/Co trilayers and Co/Ni bilayers, grown epitaxially on Cu(0 0 1). In the former system three different Fe thickness regions with different magnetic properties of the Fe layer have been observed. The Fe spin moment as a function of Fe and Ni layer thickness has been quantitatively evaluated. Below 4 ML and above $\approx$12 ML Fe thickness ferromagnetic phases with Fe spin moments of $\approx$2.5 and $\approx$2.0μ_B, respectively, are found. Between 4 and $\approx$10 ML, a reduced net magnetic moment is observed, which between 4 and 6 ML Fe thickness depends also on Ni thickness. It may be due to a non-ferromagnetic configuration of fcc Fe and an antiferromagnetic coupling between Co and Ni layers with magnetically live Fe interface layers. In Co/Ni/Cu(0 0 1) a spin-reorientation transition from in-plane to out-of-plane could be quantitatively followed in two-dimensional (Co and Ni) thickness space. The easy axis of magnetization switches from in-plane at lower Ni thicknesses or higher Co thicknesses to out-of-plane at higher Ni thicknesses or lower Co thicknesses. The formation of perpendicularly magnetized domains with decreasing size upon approaching the spin reorientation transition is explained by magnetostatic stray field energy minimization for decreasing domain wall energy.

In conclusion, microspectroscopy of wedges or crossed double wedges can help significantly in the magnetic characterization of layered systems. The microscopic spatial resolution of the quantitative magnetic information opens the way for the investigation of magnetic microstructures and microscopic domain structures by XMCD. The microspectroscopic evaluation of not only the spin moments but also the orbital moments [33] can help to characterize magnetic anisotropies on a microscopic scale, taking advantage of the relation between magnetocrystalline anisotropy and the anisotropy of the orbital moment [13,14].

Acknowledgements

We are grateful for financial support by BMBF (no. 05 SL8EF1 9), JSPS, and DFG (no. Ki 358/3-1 and 446 JAP-113/179/0). We would like to thank B. Zada for assistance in shipping the equipment and for dealing with custom's procedures. The experiments were performed at SPring-8 with the approval and financial support of JASRI (no. 1999A0319-NS -np). Our special thank is for the SPring-8 staff, in particular Y. Saitoh and R.-J. Jung, for generous help during the beamtime.

References

[1] J. Stöhr, Y. Wu, M.G. Samant, B.B. Hermsmeier, G. Harp, S. Koranda, D. Dunham, B.P. Tonner, Science 259 (1993) 658.

[2] W. Swiech, G.H. Fecher, Ch. Ziethen, O. Schmidt, G. Schönhense, K. Grzelakowski, C.M. Schneider, R. Frömter,

H.P. Oepen, J. Kirschner, J. Electron Spectrosc. Relat. Phenom. 84 (1997) 171.
[3] W. Kuch, R. Frömter, J. Gilles, D. Hartmann, Ch. Ziethen, C.M. Schneider, G. Schönhense, W. Swiech, J. Kirschner, Surf. Rev. Lett. 5 (1998) 1241.
[4] J.L. Erskine, E.A. Stern, Phys. Rev. B 12 (1975) 5016.
[5] G. Schütz, W. Wagner, W. Wilhelm, P. Kienle, R. Zeller, R. Frahm, G. Materlik, Phys. Rev. Lett. 58 (1987) 737.
[6] B.T. Thole, P. Carra, F. Sette, G. van der Laan, Phys. Rev. Lett. 68 (1992) 1943.
[7] P. Carra, B.T. Thole, M. Altarelli, X. Wang, Phys. Rev. Lett. 70 (1993) 694.
[8] C.T. Chen, Y.U. Idzerda, H.-J. Lin, N.V. Smith, G. Meigs, E. Chaban, G.H. Ho, E. Pellegrin, F. Sette, Phys. Rev. Lett. 75 (1995) 152.
[9] J. Stöhr, J. Electron Spectrosc. Relat. Phenom. 75 (1995) 253.
[10] R. Wu, A.J. Freeman, Phys. Rev. Lett. 73 (1994) 1994.
[11] W.L. O'Brien, B.P. Tonner, G.R. Harp, S.S.P. Parkin, J. Appl. Phys. 76 (1994) 6462.
[12] Y.U. Idzerda, C.T. Chen, H.-J. Lin, H. Tjeng, G. Meigs, Physica B 208–209 (1995) 746.
[13] P. Bruno, Phys. Rev. B 39 (1989) 865.
[14] G. van der Laan, J. Phys.: Cond. Matt. 10 (1998) 3239.
[15] Y. Saitoh, T. Nakatani, T. Matsushita, T. Miyahara, M. Fujisawa, K. Soda, T. Muro, S. Ueda, H. Harada, A. Sekiyama, S. Imada, H. Daimon, S. Suga, J. Synchrotron Rad. 5 (1998) 542.
[16] Y. Saitoh, H. Kimura, Y. Suzuki, T. Nakatani, T. Matsushita, T. Muro, T. Miyahara, M. Fujisawa, K. Soda, S. Ueda, H. Harada, M. Kotsugi, A. Sekiyama, S. Suga, Rev. Sci. Instrum. 71 (2000) 3254.
[17] FOCUS GmbH, http://www.focus-gmbh.com.
[18] PCO Computer Optics GmbH, http://www.pco.de.
[19] W. Kuch, M. Salvietti, X. Gao, M.-T. Lin, M. Klaua, J. Barthel, C.V. Mohan, J. Kirschner, Phys. Rev. B 58 (1998) 8556.
[20] W.L. O'Brien, B.P. Tonner, Surf. Sci. 334 (1995) 10.
[21] W.L. O'Brien, B.P. Tonner, Phys. Rev. B 52 (1995) 15332.
[22] E.J. Escorcia-Aparicio, R.K. Kawakami, Z.Q. Qiu, Phys. Rev. B 54 (1996) 4155.
[23] J. Thomassen, F. May, B. Feldmann, M. Wuttig, H. Ibach, Phys. Rev. Lett. 69 (1992) 3831.
[24] D. Li, M. Freitag, J. Pearson, Z.Q. Qiu, S.D. Bader, Phys. Rev. Lett. 72 (1994) 3112.
[25] M. Straub, R. Vollmer, J. Kirschner, Phys. Rev. Lett. 77 (1996) 743.
[26] W. Kuch, J. Gilles, F. Offi, S. S. Kang, S. Imada, S. Suga, J. Kirschner, J. Electron Spectrosc. Relat. Phenom. 109 (2000) 249.
[27] R. Nakajima, J. Stöhr, Y.U. Idzerda, Phys. Rev. B 59 (1999) 6421.
[28] F. Huang, M.T. Kief, G.J. Mankey, R.F. Willis, Phys. Rev. B 49 (1994) 3962.
[29] W.L. O'Brien, B.P. Tonner, Phys. Rev. B 49 (1994) 15370.
[30] B. Schulz, K. Baberschke, Phys. Rev. B 50 (1994) 13467.
[31] P. Krams, F. Lauks, R.L. Stamps, B. Hillebrands, G. Güntherodt, Phys. Rev. Lett. 69 (1992) 3674.
[32] M. Kowalewski, C.M. Schneider, B. Heinrich, Phys. Rev. B 47 (1993) 8748.
[33] W. Kuch, J. Gilles, S.S. Kang, S. Imada, S. Suga, J. Kirschner, Phys. Rev. B 62 (2000) 3824.
[34] Y. Yafet, E.M. Gyorgy, Phys. Rev. B 38 (1988) 9145.
[35] M. Speckmann, H.P. Oepen, H. Ibach, Phys. Rev. Lett. 75 (1995) 2035.